Pet.Sci.(2012)9:485-497
DOI 10.1007/s12182-012-0233-6

A control volume based finite element method for simulating incompressible two-phase flow in heterogeneous porous media and its application to reservoir engineering

SADRNEJAD S A[1], GHASEMZADEH H[1], GHOREISHIAN AMIRI S A[1]* and MONTAZERI G H[2]

[1] Faculty of Civil Engineering, K. N. Toosi University of Technology, Tehran, Iran
[2] Research and Development Department, Iranian Central Oil Field Co., Tehran, Iran

Abstract: Applying the standard Galerkin finite element method for solving flow problems in porous media encounters some difficulties such as numerical oscillation at the shock front and discontinuity of the velocity field on element faces. Discontinuity of velocity field leads this method not to conserve mass locally. Moreover, the accuracy and stability of a solution is highly affected by a non-conservative method. In this paper, a three dimensional control volume finite element method is developed for two-phase fluid flow simulation which overcomes the deficiency of the standard finite element method, and attains high-orders of accuracy at a reasonable computational cost. Moreover, this method is capable of handling heterogeneity in a very rational way. A fully implicit scheme is applied to temporal discretization of the governing equations to achieve an unconditionally stable solution. The accuracy and efficiency of the method are verified by simulating some waterflooding experiments. Some representative examples are presented to illustrate the capability of the method to simulate two-phase fluid flow in heterogeneous porous media.

Key words: Finite element method, control volume, two-phase flow, heterogeneity, porous media, waterflooding

1 Introduction

Simulation of mass transport and fluid flow in porous media is a problem of increasing importance in engineering. Among the practical applications of mass transport in porous media, groundwater flow, oil recovery and enhanced oil recovery processes, contaminant transport in ground water and vadose zone could be mentioned.

One of the main objectives of simulating multiphase flow in porous media is to properly capture the complex geometry and heterogeneity of rocks. Rock properties, such as porosity and permeability, may change significantly from one region to another, and subsequently, fluid velocity will vary by several orders of magnitude over a relatively short distance. Due to these facts, multiphase flow simulation in porous media poses a great challenge for most of the available numerical methods.

Various numerical methods have been applied to solve the governing equations describing subsurface flow. The finite difference (FD) method has been widely used in the solution of these equations (Todd et al, 1972; Settari and Aziz, 1975; Abriola and Pinder, 1985; Chen and Ewing, 1997; Chen et al, 2005; Lu and Wheeler, 2009). However, this method produces excessive numerical dispersion and grid orientation problems (Ewing, 1983) in addition to difficulties in the treatment of complicated geometry and boundary conditions. Intrinsic mesh flexibility of the finite element method (FEM) could overcome these deficiencies, but the classical FEM is not, in general, locally mass conservative (Chen et al, 2006b), and tends to generate numerical solutions with severe nonphysical oscillations (Wang et al, 2003).

Recently, mass conservative schemes such as the unstructured finite volume methods (FVM), mixed finite-element method (MFEM) and combination of finite element and the finite volume methods (FEFVM) have been extensively developed and studied in the literature (Durlofsky, 1994; Verma, 1996; Bergamaschi et al, 1998; Edwards and Rogers, 1998; Edwards, 2002; Korsawe et al, 2003; Rees et al, 2004; Nayagum et al, 2004; Geiger et al, 2004; Hoteit and

*Corresponding author. email: sa_ghoreishian@dena.kntu.ac.ir
Received December 2, 2011

Firoozabadi, 2005; Carvalho et al, 2007).

Another interesting approach is the control volume finite element method (CVFEM) which has been developed as a fully conservative method. Application of CVFEM to simulate multiphase fluid flow in porous media has been rapidly increased (Fung et al, 1991; Li et al, 2003; Chen et al, 2006b; Mello et al, 2009), since this method combines the mesh flexibility of FEM with the local conservative characteristic of the finite difference method at the control volume level.

Another important object in the field of multiphase flow simulation is to develop a stable, efficient, robust, and accurate solution for solving the multiphase flow equations in the time domain. Three types of time discretization method are commonly used to solve these equations: the IMPES (implicit pressure and explicit saturation) method; the sequential method; and the fully implicit method (Chen et al, 2006a). The IMPES solution method makes the pressure variables implicit in time, whereas, the saturation variables are considered explicit in time. This method of solution has a stability limit that is inversely proportional to the fluid velocity, and this limitation is often too restrictive in practice. The sequential solution method attempts to remedy the problem, firstly, by solving the pressure equations based on the results of the last time step, secondly, by computing the new fluids velocity fields based on the new pressure and finally solving the transport problem based on the updated velocities. In the absence of capillarity, the stability limitation of the sequential method is less than the IMPES method; however, decoupling of equations in this method could generate mass balance errors that are proportional to the length of time steps. Finally, the fully implicit method solves the system of coupled equations simultaneously with an implicit time scheme. This method is unconditionally stable and can take large time steps.

The main goal of this paper is to present a fully conservative method for solving two-phase flow equations which could handle heterogeneities in a rational way. In order to avoid any stability limitation, a fully implicit scheme is applied to temporal discretization of the governing equations. The accuracy and efficiency of the proposed method are verified by comparing the model results with some waterflooding experiments. Furthermore, in order to evaluate the model capability for handling discontinuous materials properties, some representative examples are presented.

2 Governing equations

The system of concern in this paper is considered as a mixture consisting of a rigid porous media, water and oil which are considering as wetting and non-wetting phases, respectively. It is assumed that oil and water are two immiscible and incompressible fluids. The basic equations for describing this system are derived based on the classical continuum theory of mixture (Goodman and Gowin, 1972). In this approach, the constituents of the mixture are considered as overlapping continua. This means that each point in the mixture is simultaneously occupied by materials of all phases.

The flow of each phase is described by conservation of mass

$$\rho_\alpha \frac{\partial n_\alpha}{\partial t} + \nabla.(n_\alpha \rho_\alpha \boldsymbol{w}_\alpha) = \dot{M}_\alpha \tag{1}$$

and generalized Darcy's law

$$n_\alpha \boldsymbol{w}_\alpha = \frac{k_{r\alpha}\boldsymbol{K}}{\mu_\alpha}\left[\rho_\alpha \boldsymbol{g} - \nabla p_\alpha\right] \tag{2}$$

where n_α represents the volume fraction of phase α [α denotes water (w) and oil (o)]; ρ_α is the mass density of phase α; $\boldsymbol{w}_\alpha$ is the relative velocity of phase α with respect to the solid skeleton; M_α is the sources or sinks terms; $\boldsymbol{K}$ is the absolute permeability tensor of the solid skeleton; $k_{r\alpha}$ and μ_α are the relative permeability and the dynamic viscosity of phase α, respectively. The relative permeability for water and oil phases are calculated by the relations proposed by Lujan (1985)

$$k_{rw} = S_{ew}^{(2+3\lambda)/\lambda} \tag{3a}$$

$$k_{ro} = (1 - S_{ew})^2 (1 - S_{ew}^{(2+\lambda)/\lambda}) \tag{3b}$$

where S_{ew} ($S_{ew} = \dfrac{n_w - n_{w_{res}}}{n_{w_{sat}} - n_{w_{res}}}$) denotes the effective degree of saturation of water phase and λ is a fitting parameter related to the pore size distribution.

In addition, there is a constraint between fluid volume fractions

$$n_w + n_o = n \tag{4}$$

where n represents the rock porosity. This relation means that the fluid phases jointly fill the voids.

Another constraint equation is defined by considering the fact that when two fluid phases flow in a porous medium, flow of each phase is affected by the other phase. In order to specify this interacting motion in the model, one requires equations which link each phase pressure to its volume fraction. The most practical method for considering this interacting motion is to use empirical correlations relating the capillary pressure (p_c) to the volume fraction of the wetting phase (Hassanizadeh and Gray, 1993). In this paper, the relation proposed by Brooks and Corey (1966) is employed

$$n_w = n_{w_{res}} + \left(n_{w_{sat}} - n_{w_{res}}\right)\left[\frac{p_d}{p_c}\right]^\lambda \tag{5}$$

where $n_{w_{sat}}$ is the value of water volume fraction at zero suction; $n_{w_{res}}$ is the value of water volume fraction at very high suction; p_d is the displacement pressure for oil; and λ is defined in the relative permeability relations (Eq. 3).

Partially differentiating Eq. (5), one obtains

$$\mathrm{d}n_w = \frac{\mathrm{d}n_w}{\mathrm{d}p_c}\left(\mathrm{d}p_o - \mathrm{d}p_w\right) = n'_w\left(\mathrm{d}p_o - \mathrm{d}p_w\right) \tag{6}$$

and from Eq. (4)

$$\mathrm{d}n_o = -\mathrm{d}n_w \tag{7}$$

Substituting Eqs. (2), (6) and (7) into Eq. (1), the final

form of mass balance equations for water and oil phases are obtained:

$$\left(-n'_{\mathrm{w}}\rho_{\mathrm{w}}\right)\frac{\partial p_{\mathrm{w}}}{\partial t}+\left(n'_{\mathrm{w}}\rho_{\mathrm{w}}\right)\frac{\partial p_{\mathrm{o}}}{\partial t} +\nabla.\left\{\rho_{\mathrm{w}}\boldsymbol{K}_{\mathrm{w}}\left[\rho_{\mathrm{w}}\boldsymbol{g}-\nabla p_{\mathrm{w}}\right]\right\}-\dot{M}_{\mathrm{w}}=0 \tag{8}$$

$$\left(-n'_{\mathrm{w}}\rho_{\mathrm{o}}\right)\frac{\partial p_{\mathrm{o}}}{\partial t}+\left(n'_{\mathrm{w}}\rho_{\mathrm{o}}\right)\frac{\partial p_{\mathrm{w}}}{\partial t} +\nabla.\left\{\rho_{\mathrm{o}}\boldsymbol{K}_{\mathrm{o}}\left[\rho_{\mathrm{o}}\boldsymbol{g}-\nabla p_{\mathrm{o}}\right]\right\}-\dot{M}_{\mathrm{o}}=0 \tag{9}$$

where $\boldsymbol{K}_\alpha$ ($\boldsymbol{K}_\alpha=\frac{k_{\mathrm{r}\alpha}\boldsymbol{K}}{\mu_\alpha}$) is the mobility of phase α. It is worth noting that viscosities of water and oil phases are assumed to be pressure independent.

Eqs. (8) and (9) represent a system of two highly nonlinear partial differential equations. Relative permeability and phase volume fractions are the major nonlinearity sources in these equations.

In this paper, phase pressures are selected as the primary unknowns. Choice of the primary variables is a crucial step in efficiency of multiphase flow models in porous media (Wua and Forsyth, 2001). Ataie-Ashtiani and Raeesi-Ardekani (2010) showed that selection of the phase pressures as the primary variables tends to minimize computational cost. However, Wua and Forsyth (2001) did not agree with them. On the other hand, this work is the first step towards the development of more general numerical algorithm for the coupled hydro-mechanical simulation of multi-phase flow in porous media. Therefore, based on some of the recent hydro-mechanical models (Lewis et al, 1998; Pao et al, 2001; Li et al, 2005), in this paper, the phase pressures are chosen as the primary variables.

The equations in this system are strongly coupled. Capillary pressure plays a key role in this type of formulation, because coupling of Eqs. (8) and (9) is due to existence of capillarity. Moreover, fluid saturation is calculated based on the existence of capillary pressure function. Theoretically, this system of equations collapses at the absence of an oil phase, because two pressures are no longer independent, and at the same time two mass balance equations are still needed to be solved. While applying this situation in the model, if p_{c} is defined with a certain value equaling to p_{d} in the capillary pressure relation (Eq. (5)), water and oil pressures will remain independent and the problem will be solved automatically.

In order to complete the description of governing equations, it is necessary to define appropriate initial and boundary conditions. The initial conditions specify the full field of water and oil phase pressures at time t=0

$$p_\alpha=p_\alpha^0 \quad \text{in } \Omega \text{ and on } \Gamma \tag{10}$$

where Ω is the domain of interest and Γ is its boundary. The boundary condition can be of two types or a combination of these: the Dirichlet boundary condition, in which the phase pressures on the boundaries (Γ_p) are known, and the Neumann boundary condition, in which the values of phase fluxes at the boundaries (Γ_q) are imposed (where $\Gamma=\Gamma_p\bigcup\Gamma_q$)

$$p_\alpha=\bar{p}_\alpha \quad \text{on } \Gamma_p \tag{11}$$

$$\left\{\rho_\alpha\boldsymbol{K}_\alpha\left[\rho_\alpha\boldsymbol{g}-\nabla p_\alpha\right]\right\}^{\mathrm{T}}\cdot\boldsymbol{n}=\bar{\boldsymbol{q}}_\alpha \quad \text{on } \Gamma_q \tag{12}$$

where $\boldsymbol{n}$ denotes the outward unit normal vector on the boundary and $\bar{\boldsymbol{q}}$ is the imposed mass flux normal to the boundary.

3 Numerical solution

In the present work, a CVFEM is adopted for numerical solution of Eqs. (8) and (9) in spatial domain. As common in FEM, the discrete form of differential equations is presented in a transformed space with local coordinate system (ξ,η,ζ) defined for each element (Fig. 1). In the proposed method, the physical domain discretization is done using hexahedral elements. And further subdivision of elements into control volumes is performed in the transformed space, as shown in Fig. 2. The coordinate transformation at the element level is performed by

$$x_i(\xi,\eta,\zeta)=\boldsymbol{N}(\xi,\eta,\zeta)\hat{\boldsymbol{x}}_i \qquad i=1,2,3 \tag{13}$$

where x_i is the value of the ith coordinate in the physical space; $\boldsymbol{N}$ is the vector of standard finite element shape functions and $\hat{\boldsymbol{x}}_i$ is the nodal value vector of the ith coordinate.

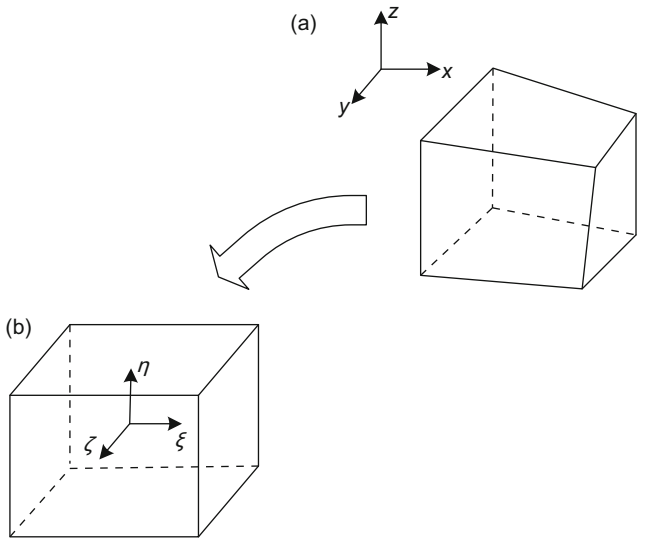

Fig. 1 Element representation
(a) in physical domain and (b) in the transformed space

The control volume finite element discretization of Eqs. (8) and (9) is expressed in terms of the nodal phase pressures, i.e. $\hat{\boldsymbol{p}}_\alpha$, which are selected as the primary variables. The values of phase pressures (p_α) at any point within an element are

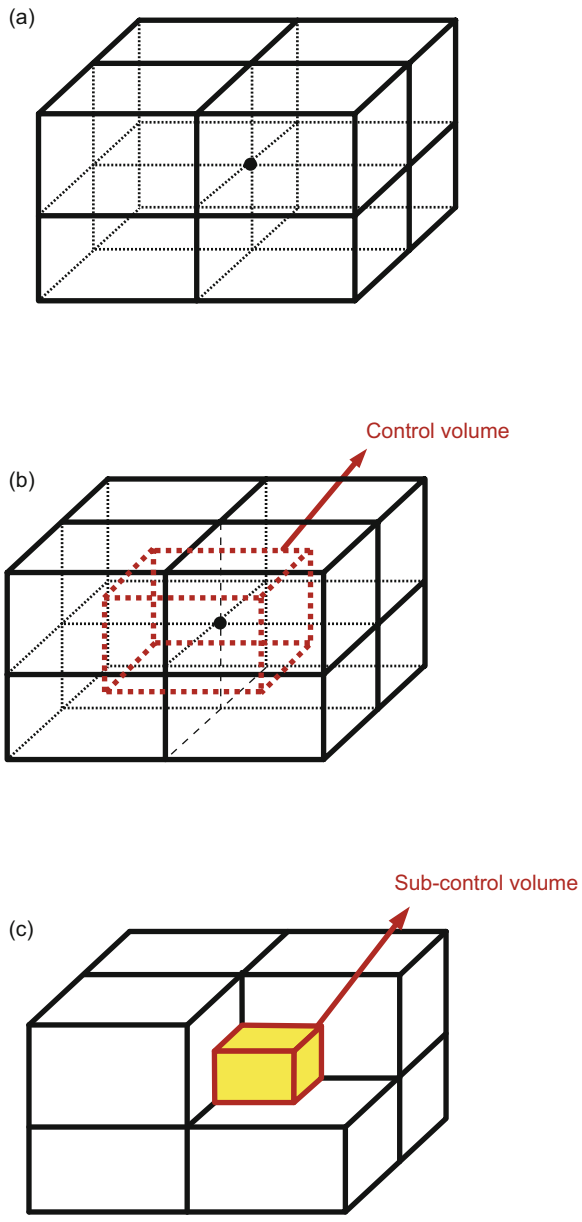

Fig. 2 (a) System of finite element mesh in the transformed space, (b) control volume representation around a node and (c) illustrating a sub-control volume belongs to the eliminated element

approximated by the following expressions

$$p_{\mathrm{w}}(\xi,\eta,\zeta)=\boldsymbol{N}(\xi,\eta,\zeta)\hat{\boldsymbol{p}}_{\mathrm{w}} \tag{14a}$$

$$p_{\mathrm{o}}(\xi,\eta,\zeta)=\boldsymbol{N}(\xi,\eta,\zeta)\hat{\boldsymbol{p}}_{\mathrm{o}} \tag{14b}$$

In the classical FEM, the first order polynomials are commonly used as the shape functions. This lead the pressure field to be continued in the whole physical space; but the velocity field will be discontinuous between adjacent elements. However, because the control volume faces are located inside the elements, the velocity fields are continues between adjacent control volumes (Fig. 3). It means that the mass out-flux through a surface of an element is not necessarily equal to the mass in-flux through the same surface of the adjacent element; and subsequently mass does not conserve at the element level (Fig. 4(a)). However, owing to continuity of the velocity field at the control volume faces, if the mass flux is integrated on each control volume surface, conservation of mass will be obtained on the control volumes (Durlofsky, 1994) (Fig. 4(b)).

Now, by integrating Eqs. (8) and (9) over a control volume and applying Gauss theorem, the weak form of balance equations are derived

$$\begin{aligned}&\int_{\Omega_{\mathrm{C.V.}}}\left(-n'_{\mathrm{w}}\rho_{\mathrm{w}}\right)\frac{\partial p_{\mathrm{w}}}{\partial t}\mathrm{d}\Omega+\int_{\Omega_{\mathrm{C.V.}}}\left(n'_{\mathrm{w}}\rho_{\mathrm{w}}\right)\frac{\partial p_{\mathrm{o}}}{\partial t}\mathrm{d}\Omega\\&+\int_{\Gamma_{\mathrm{C.V.}}}\left\{\rho_{\mathrm{w}}\boldsymbol{K}_{\mathrm{w}}\left[\rho_{\mathrm{w}}\boldsymbol{g}-\nabla p_{\mathrm{w}}\right]\right\}^{\mathrm{T}}\cdot\boldsymbol{n}\,\mathrm{d}\Gamma-\int_{\Omega_{\mathrm{C.V.}}}\dot{M}_{W}\,\mathrm{d}\Omega=0\end{aligned} \tag{15}$$

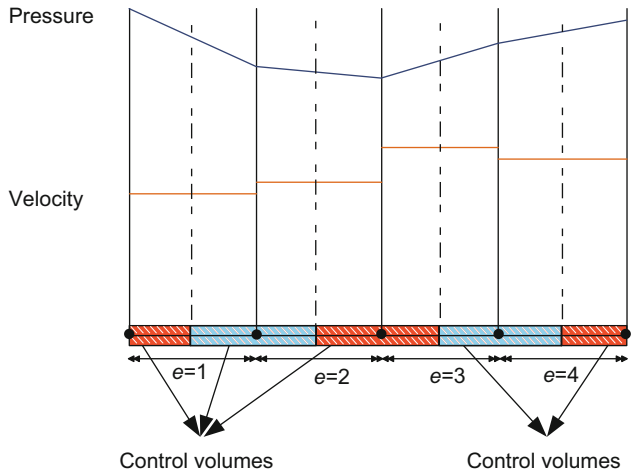

Fig. 3 Discontinuity of the velocity field across the element faces and continuity of the velocity field across the control volume faces for the one-dimensional finite element mesh

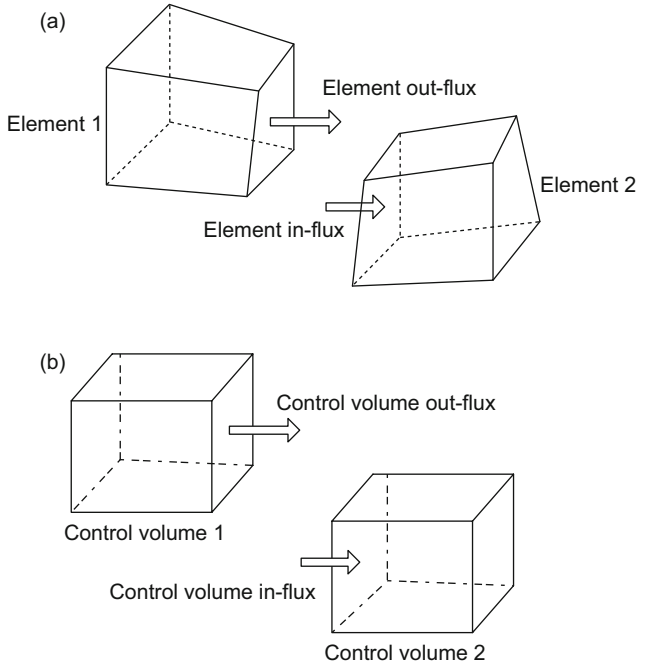

Fig. 4 Mass in-flux and out-flux through the elements and control volumes faces (a) mass out-flux from element 1 is not necessarily equal to mass in-flux into element 2 and (b) mass out-flux from control volnme 1 is always equal to mass in-flux into control 2 volume

$$\int_{\Omega_{C.V.}}\left(-n'_{w}\rho_{o}\right)\frac{\partial p_{o}}{\partial t}\mathrm{d}\Omega+\int_{\Omega_{C.V.}}\left(n'_{w}\rho_{o}\right)\frac{\partial p_{w}}{\partial t}d\Omega$$
$$+\int_{\Gamma_{C.V.}}\left\{\rho_{o}\boldsymbol{K}_{o}\left[\rho_{o}\boldsymbol{g}-\nabla p_{o}\right]\right\}^{T}\cdot\boldsymbol{n}\,\mathrm{d}\Gamma-\int_{\Omega_{C.V.}}\dot{M}_{o}\,\mathrm{d}\Omega=0 \tag{16}$$

where $\Omega_{C.V.}$ indicates the domain of a control volume bounded by $\Gamma_{C.V.}$.

Substituting the interpolatory representation of phase pressures (Eq. (14)) into Eqs. (15) and (16), one obtains

$$\left[\int_{\Omega_{C.V.}}\left(-n'_{w}\rho_{w}\right)\boldsymbol{N}\,\mathrm{d}\Omega\right]\frac{\partial\hat{\boldsymbol{p}}_{w}}{\partial t}+\left[\int_{\Omega_{C.V.}}\left(n'_{w}\rho_{w}\right)\boldsymbol{N}\,\mathrm{d}\Omega\right]\frac{\partial\hat{\boldsymbol{p}}_{o}}{\partial t}$$
$$-\left[\int_{\Gamma_{C.V.}}\left\{\rho_{w}\boldsymbol{K}_{w}\nabla\boldsymbol{N}\right\}^{T}\cdot\boldsymbol{n}\,\mathrm{d}\Gamma\right]\hat{\boldsymbol{p}}_{w} \tag{17}$$
$$=\int_{\Omega_{C.V.}}\dot{M}_{w}\,\mathrm{d}\Omega-\int_{\Gamma_{C.V.}}\rho_{w}^{2}\left(\boldsymbol{K}_{w}\boldsymbol{g}\right)^{T}\cdot\boldsymbol{n}\,\mathrm{d}\Gamma$$

$$\left[\int_{\Omega_{C.V.}}\left(-n'_{w}\rho_{o}\right)\boldsymbol{N}\,\mathrm{d}\Omega\right]\frac{\partial\hat{\boldsymbol{p}}_{o}}{\partial t}+\left[\int_{\Omega_{C.V.}}\left(n'_{w}\rho_{o}\right)\boldsymbol{N}\,\mathrm{d}\Omega\right]\frac{\partial\hat{\boldsymbol{p}}_{w}}{\partial t}$$
$$-\left[\int_{\Gamma_{C.V.}}\left\{\rho_{o}\boldsymbol{K}_{o}\nabla\boldsymbol{N}\right\}^{T}\cdot\boldsymbol{n}\,\mathrm{d}\Gamma\right]\hat{\boldsymbol{p}}_{o} \tag{18}$$
$$=\int_{\Omega_{C.V.}}\dot{M}_{o}\,\mathrm{d}\Omega-\int_{\Gamma_{C.V.}}\rho_{o}^{2}\left(\boldsymbol{K}_{o}\boldsymbol{g}\right)^{T}\cdot\boldsymbol{n}\,\mathrm{d}\Gamma$$

For the boundary nodes, at least one face of the associated control volume lies on the physical boundary. The boundary conditions must be implemented to the model at these nodes. Dirichlet boundary conditions (Eq. (11)) are enforced by direct substitution of prescribed nodal values, as in the classical FEM. For Newman boundary conditions (Eq. (12)), the prescribed fluxes through the physical boundaries are added to the right hand side of the equations. Consequently, Eqs. (17) and (18) will have the form

$$\left[\int_{\Omega_{C.V.}}\left(-n'_{w}\rho_{w}\right)\boldsymbol{N}\,\mathrm{d}\Omega\right]\frac{\partial\hat{\boldsymbol{p}}_{w}}{\partial t}+\left[\int_{\Omega_{C.V.}}\left(n'_{w}\rho_{w}\right)\boldsymbol{N}\,\mathrm{d}\Omega\right]\frac{\partial\hat{\boldsymbol{p}}_{o}}{\partial t}$$
$$-\left[\int_{\Gamma_{C.V.}-\Gamma_{q}}\left\{\rho_{w}\boldsymbol{K}_{w}\nabla\boldsymbol{N}\right\}^{T}\cdot\boldsymbol{n}\,\mathrm{d}\Gamma\right]\hat{\boldsymbol{p}}_{w} \tag{19}$$
$$=\int_{\Omega_{C.V.}}\dot{M}_{w}\,\mathrm{d}\Omega-\int_{\Gamma_{q}}\overline{q}_{w}\,\mathrm{d}\Gamma-\int_{\Gamma_{C.V.}-\Gamma_{q}}\rho_{w}^{2}\left(\boldsymbol{K}_{w}\boldsymbol{g}\right)^{T}\cdot\boldsymbol{n}\,\mathrm{d}\Gamma$$

$$\left[\int_{\Omega_{C.V.}}\left(-n'_{w}\rho_{o}\right)\boldsymbol{N}\,\mathrm{d}\Omega\right]\frac{\partial\hat{\boldsymbol{p}}_{o}}{\partial t}+\left[\int_{\Omega_{C.V.}}\left(n'_{w}\rho_{o}\right)\boldsymbol{N}\,\mathrm{d}\Omega\right]\frac{\partial\hat{\boldsymbol{p}}_{w}}{\partial t}$$
$$-\left[\int_{\Gamma_{C.V.}-\Gamma_{q}}\left\{\rho_{o}\boldsymbol{K}_{o}\nabla\boldsymbol{N}\right\}^{T}\cdot\boldsymbol{n}\,\mathrm{d}\Gamma\right]\hat{\boldsymbol{p}}_{o} \tag{20}$$
$$=\int_{\Omega_{C.V.}}\dot{M}_{o}d\Omega-\int_{\Gamma_{q}}\overline{q}_{o}d\Gamma-\int_{\Gamma_{C.V.}-\Gamma_{q}}\rho_{o}^{2}\left(\boldsymbol{K}_{o}\boldsymbol{g}\right)^{T}\cdot\boldsymbol{n}\,\mathrm{d}\Gamma$$

Eqs. (19) and (20) present the discretized form of the balance equations at the control volume level. On the other hand, representation of the equations at the element level could help the model to handle probable discontinuous material properties in the physical domain (see Section 4). To aim this goal, each control volume around a node is divided to some sub-control volumes belonging to different elements associated with the node (Fig. 2). Similarly, each face of a control volume is divided to some sub-control volume faces. Hence, integrations over a control volume or a control volume face could be calculated by summing up the individual integrations over the sub-control volumes and the sub-control volume faces. By applying this methodology, discretized formulation could be represented at the element level and the complete balance equations could be obtained by assembling the element-wise equations, as in the classical FEM. The element-wise representation of Eqs. (19) and (20) is

$$\begin{bmatrix}\overline{\boldsymbol{P}}_{ww} & 0\\ 0 & \overline{\boldsymbol{P}}_{oo}\end{bmatrix}\begin{bmatrix}\hat{\boldsymbol{p}}_{w}\\ \hat{\boldsymbol{p}}_{o}\end{bmatrix}+\begin{bmatrix}\boldsymbol{P}_{ww} & \boldsymbol{C}_{wo}\\ \boldsymbol{C}_{ow} & \boldsymbol{P}_{oo}\end{bmatrix}\frac{\mathrm{d}}{\mathrm{d}t}\begin{bmatrix}\hat{\boldsymbol{p}}_{w}\\ \hat{\boldsymbol{p}}_{o}\end{bmatrix}=\begin{bmatrix}\boldsymbol{f}_{w}\\ \boldsymbol{f}_{o}\end{bmatrix} \tag{21}$$

where the coefficients are described as

$$\overline{\boldsymbol{P}}_{ww}=-\int_{\Gamma_{S.C.V.}-\Gamma_{q}}\boldsymbol{W}^{T}\left\{\left(\rho_{w}\boldsymbol{K}_{w}\nabla\boldsymbol{N}\right)^{T}\cdot\boldsymbol{n}\right\}^{T}\mathrm{d}\Gamma \tag{22a}$$

$$\overline{\boldsymbol{P}}_{oo}=-\int_{\Gamma_{S.C.V.}-\Gamma_{q}}\boldsymbol{W}\left\{\left(\rho_{o}\boldsymbol{K}_{o}\nabla\boldsymbol{N}\right)^{T}\cdot\boldsymbol{n}\right\}^{T}\mathrm{d}\Gamma \tag{22b}$$

$$\boldsymbol{P}_{ww}=\int_{\Omega_{e}}\boldsymbol{W}^{T}\left(-n'_{w}\rho_{w}\right)\boldsymbol{N}\,\mathrm{d}\Omega \tag{22c}$$

$$\boldsymbol{P}_{oo}=\int_{\Omega_{e}}\boldsymbol{W}^{T}\left(-n'_{w}\rho_{o}\right)\boldsymbol{N}\,\mathrm{d}\Omega \tag{22d}$$

$$\boldsymbol{C}_{wo}=\int_{\Omega_{e}}\boldsymbol{W}^{T}\left(n'_{w}\rho_{w}\right)\boldsymbol{N}\,\mathrm{d}\Omega \tag{22e}$$

$$\boldsymbol{C}_{ow}=\int_{\Omega_{e}}\boldsymbol{W}^{T}\left(n'_{w}\rho_{o}\right)\boldsymbol{N}\,\mathrm{d}\Omega \tag{22f}$$

$$\boldsymbol{f}_{w}=\int_{\Omega_{e}}\dot{M}_{w}\boldsymbol{W}^{T}\,\mathrm{d}\Omega-\int_{\Gamma_{q}}\overline{q}_{w}\boldsymbol{W}^{T}\,\mathrm{d}\Gamma$$
$$-\int_{\Gamma_{S.C.V.}-\Gamma_{q}}\left[\rho_{w}^{2}\left(\boldsymbol{K}_{w}\boldsymbol{g}\right)^{T}\cdot\boldsymbol{n}\right]\boldsymbol{W}^{T}\,\mathrm{d}\Gamma \tag{22g}$$

$$\boldsymbol{f}_{o}=\int_{\Omega_{e}}\dot{M}_{o}\boldsymbol{W}^{T}\,\mathrm{d}\Omega-\int_{\Gamma_{q}}\overline{q}_{o}\boldsymbol{W}^{T}\,\mathrm{d}\Gamma$$
$$-\int_{\Gamma_{S.C.V.}-\Gamma_{q}}\left[\rho_{o}^{2}\left(\boldsymbol{K}_{o}\boldsymbol{g}\right)^{T}\cdot\boldsymbol{n}\right]\boldsymbol{W}^{T}\,\mathrm{d}\Gamma \tag{22h}$$

where Ω_{e} and $\Gamma_{S.C.V.}$ indicate the domain of an element and the area of a sub-control volume faces, respectively, and W is the vector of weighting functions. The weighting functions in this model are chosen such that the ith weighting function of an element takes a constant value of unity over the sub-control volume belonging to node i and zero elsewhere in the element, i.e.

$$W_{i}=\begin{cases}1 & \text{in the sub-control volume belongs to node } i\\ 0 & \text{otherwise}\end{cases} \tag{23}$$

The time discretization of Eq. (21) is performed by the fully implicit first order accurate finite difference scheme

$$\begin{bmatrix} \overline{\boldsymbol{P}}_{\mathrm{ww}} + \Delta t \boldsymbol{P}_{\mathrm{ww}} & \boldsymbol{C}_{\mathrm{wo}} \\ \boldsymbol{C}_{\mathrm{ow}} & \overline{\boldsymbol{P}}_{\mathrm{oo}} + \Delta t \boldsymbol{P}_{\mathrm{ww}} \end{bmatrix}_{t+1} \begin{bmatrix} \Delta \hat{\boldsymbol{p}}_{\mathrm{w}} \\ \Delta \hat{\boldsymbol{p}}_{\mathrm{o}} \end{bmatrix}_{t+1} = \Delta t \begin{bmatrix} \boldsymbol{f}_{\mathrm{w}} \\ \boldsymbol{f}_{\mathrm{o}} \end{bmatrix}_{t+1} - \Delta t \begin{bmatrix} \overline{\boldsymbol{P}}_{\mathrm{ww}} & 0 \\ 0 & \overline{\boldsymbol{P}}_{\mathrm{oo}} \end{bmatrix}_{t+1} \begin{bmatrix} \hat{\boldsymbol{p}}_{\mathrm{w}} \\ \hat{\boldsymbol{p}}_{\mathrm{o}} \end{bmatrix}_{t} \tag{24}$$

where Δt is the time step length and $\Delta \hat{\boldsymbol{p}}_{n+1} = \hat{\boldsymbol{p}}_{n+1} - \hat{\boldsymbol{p}}_{n}$.

4 Heterogeneous porous media

In heterogeneous porous media, it is assumed that the change of rock properties is only acceptable on the element edges. However, smooth variation of properties is acceptable inside the elements, because it could be considered with the finite elements interpolated functions.

In general, the element-wise discretization of the equations and the above-mentioned assumption are sufficient to simulate the fluid flow in heterogeneous porous media. To achieve the mass balance equations for each control volume in the element-wise format, coefficients of Eq. (24) are integrated separately in each sub-control volume and sub-control volume faces (Fig. 5) where the rock properties are constant or changed smoothly. Then, the complete balance equations are obtained by assembling the coefficients, as usual in the classical FEM. Consequently, heterogeneity of medium could be considered easily and without any modification of the proposed formulation.

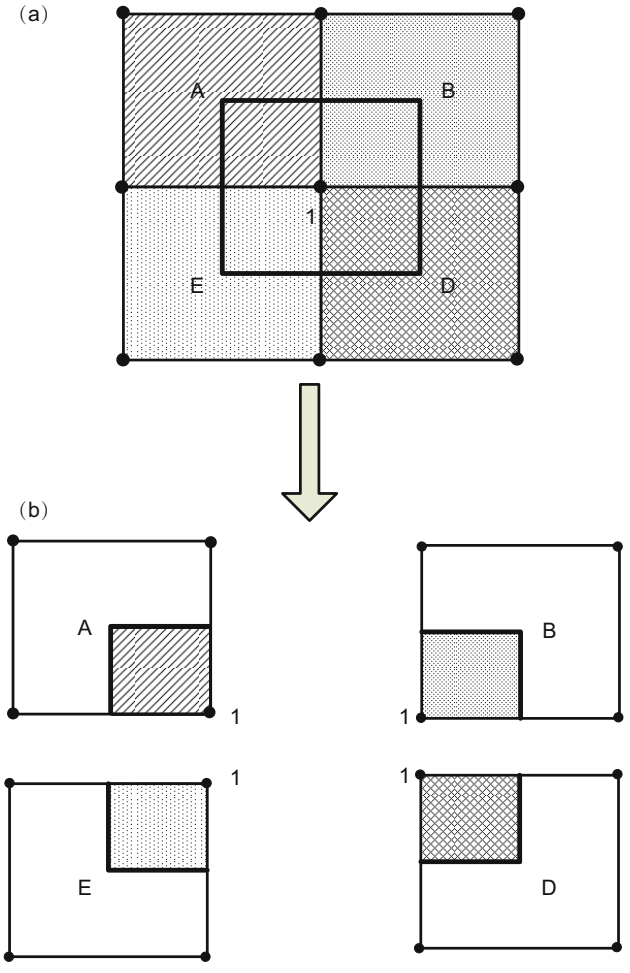

Fig. 5 2D control volume split by four different rock types

5 Model verification and examples

The accuracy and efficiency of the method are verified in this section through simulation of some waterflooding experiments which are reported by Hadia et al (2007; 2008). Furthermore, some representative examples are shown to illustrate the potential of the proposed method to simulate two-phase fluid flow in heterogeneous porous media.

5.1 One dimensional waterflooding

One-dimensional waterflooding experiments, reported by Hadia et al (2007), are selected as the first example to test the validity of the model. The selected experiments were performed at room temperature of 24 °C and atmospheric pressure. The tests were done on rectangular Berea sandstone core samples (2.5×2.4×54 cm^3) saturated with heavy liquid paraffin oil. To simulate the recovery process with waterflooding, brine (water with 1% KCl by volume) was injected into the sample at a rate of 100 and 50 mL/h. The measured viscosity of the heavy paraffin oil and brine were 130 and 0.97 cP, respectively. The measured porosity and absolute permeability of the core sample used in the experiments were 38.5% and 1584 mD, respectively. The average value of irreducible water saturation for the experiments was about 32.5%. The schematic of 1D waterflooding experiment is shown in Fig. 6.

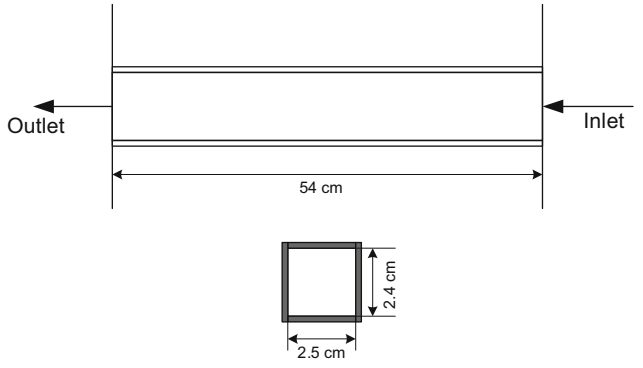

Fig. 6 Schematic of Berea sandstone core sample for 1D waterflooding experiments (Hadia et al, 2007)

The first test case (100 mL/h) is selected for calibrating of the numerical model parameters; and the latter test case is adopted to validate the model accuracy. The relative permeability and capillary curves, which are obtained from the calibration process, are shown in Figs. 7 and 8. These curves are also used for the test case with an injection rate of 50 mL/h to evaluate the model accuracy.

Fig. 9 shows the comparative curves of numerical and experimental results for recovery performance of original oil in place (OOIP). It is observed that numerical results are in agreement with experimental data. Fig. 10 shows the

distribution of water saturation inside the Berea sandstone core sample during the waterflooding test with the injection rate of 100 mL/h.

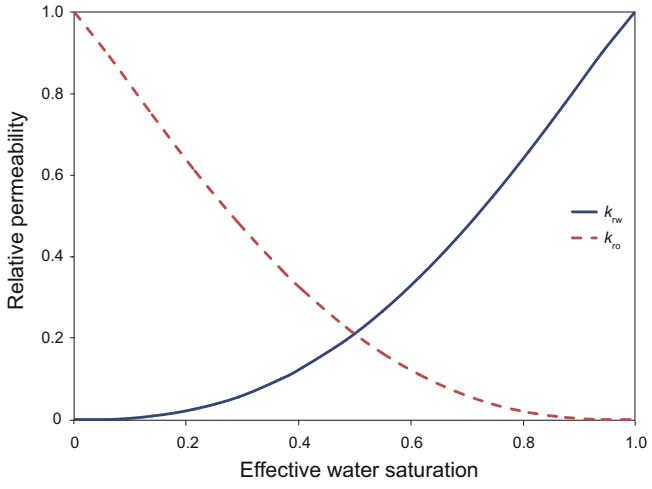

Fig. 7 Relative permeability versus effective water saturation for 1D waterflooding problem

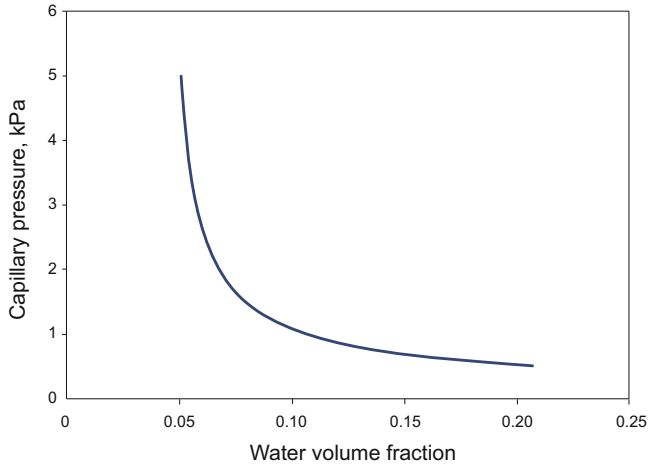

Fig. 8 Capillary pressure versus water volume fraction for 1D waterflooding problem

5.2 Three dimensional waterflooding

Hadia et al (2008) performed some three-dimensional waterflooding experiments on a sandstone outcrop of size 30×30×10 cm^3, with horizontal and vertical wells of 0.8 cm diameter drilled in the outcrop at different locations. The waterflooding tests were performed with different well configurations (vertical production-vertical injection (VP-VI) wells and horizontal production-vertical injection (HP-VI) wells) at an injection rate of 60 mL/h. The selected experiments were done at room temperature of 25±1 °C and atmosphere pressure. Water and paraffin oil were used as displacing and displaced fluids, respectively. The measured viscosity of oil and water were 130 and 0.97 cP. The measured porosity and absolute permeability of the outcrop, used in the experiments, were 20.8% and 1,500 mD, respectively. The average value of irreducible water saturation for the experiments was about 22.1%. The schematic of experiments is shown in Fig. 11.

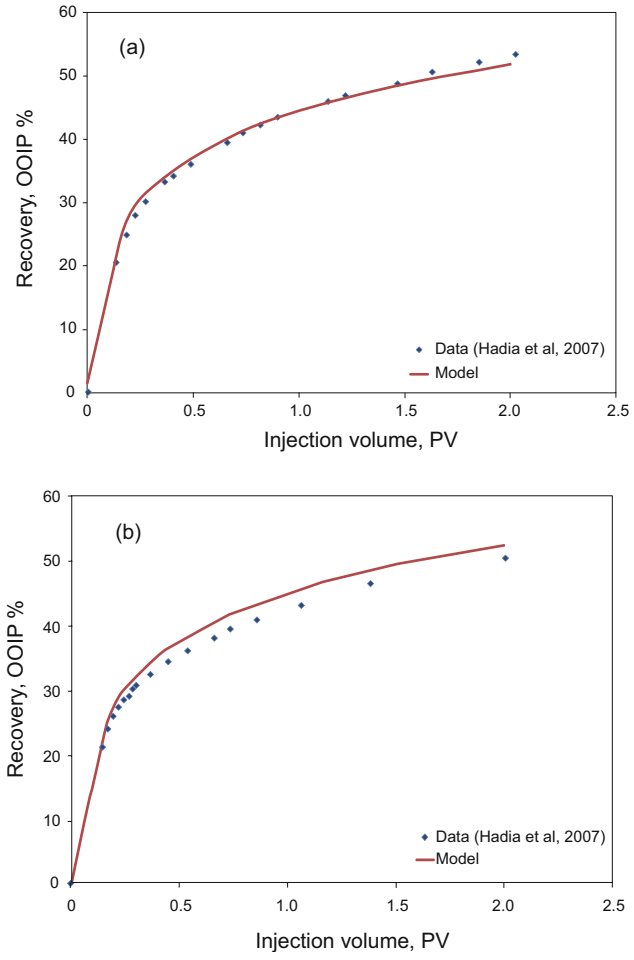

Fig. 9 Numerical and experimental results for recovery performance of OOIP (a) for an injection rate of 100 mL/h and (b) for an injection rate of 50 mL/h

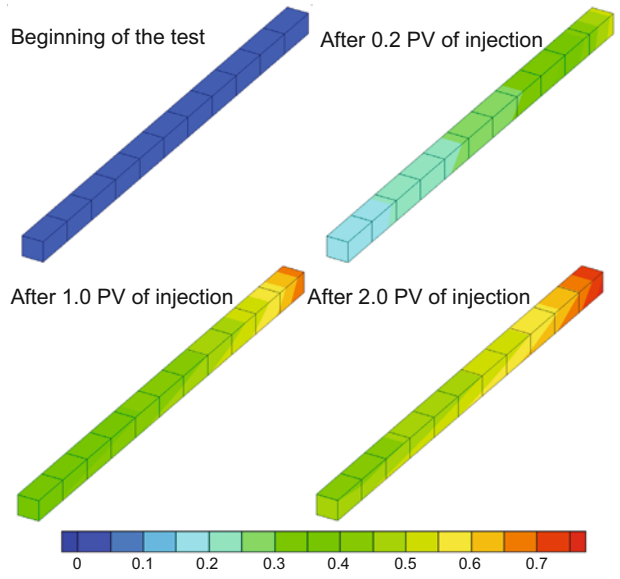

Fig. 10 Distribution of water saturation in the core sample during the test (at an injection rate of 100 mL/h)

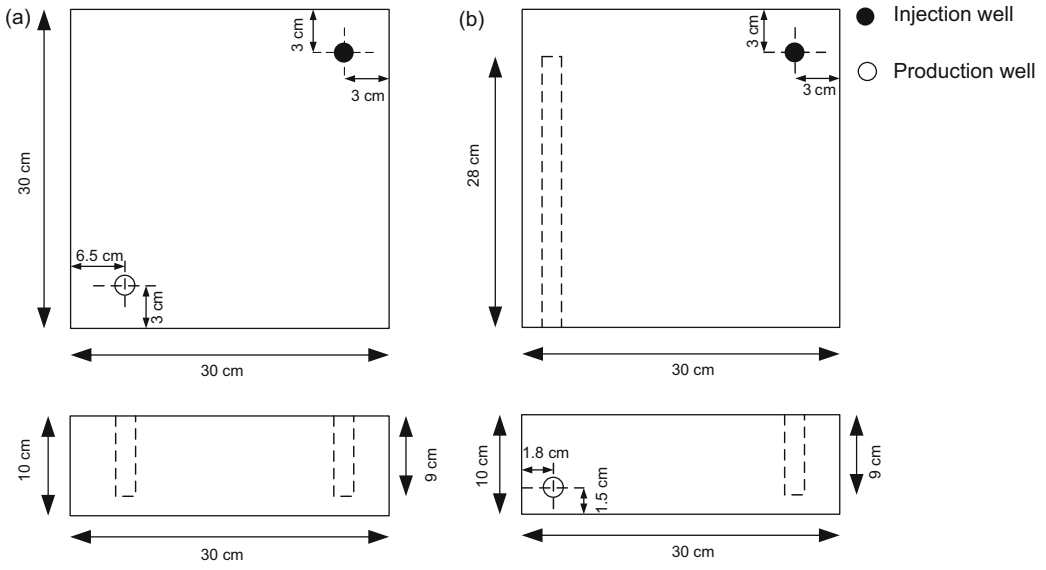

Fig. 11 Schematic of outcrop sandstone core samples (a) VP-VI wells and (b) HP-VI wells (Hadia et al, 2008)

The test with HP-VI wells is selected as the based test for calibrating the model parameters, and the test with VP-VI is used to check the model accuracy. Figs. 12 and 13 represent the relative permeability and capillary curves which are obtained from the calibration process.

The recovery performance of original oil in place (OOIP) and the percent of water in the produced fluid (water cut), resulted from the tests and numerical analyses, are compared in Figs. 14 and 15. The distribution of water saturation inside the sand stone outcrop sample during the test with HP-VI wells is presented in Fig. 16.

5.3 Solution of the elliptic pressure equation in heterogeneous domains

In order to show that the present model is capable of handling discontinuous material properties even with very coarse meshes, the simplest elliptic pressure equation ($\Delta(\boldsymbol{K}\Delta p=0$), where $\boldsymbol{K}=k\boldsymbol{I}$ and k is a scalar discontinuous coefficient) is solved in this section. This example was also adopted by Rees (2004) and Carvalho et al (2007) to show the ability of their model in the simulation of discontinuous materials. However, the model proposed by Rees (2004) produced poor results for coarse meshes, and the method proposed by Carvalho et al (2007) seems complicated for implementation.

In this example, a 1×1×1 cubic domain is considered, and two cases of material discontinuities are studied by the proposed numerical model. In the first case, the cube is split horizontally in two parts (part A and part B) as shown in Fig. 17(a), and in the second case, the cube is divided vertically into two parts (Fig. 17(b)). The non-dimensional diffusive parameters (i.e. permeability) are k_A=10 and k_B=50 for part A and B, respectively. The pressure at the top and bottom of the domain are set to p_T=0 and p_B=10, respectively. Impermeable boundary conditions are set to the lateral edges of the domain. Fig. 18 shows the extremely coarse mesh adopted for both cases of this example and the pressure contours in the cubes.

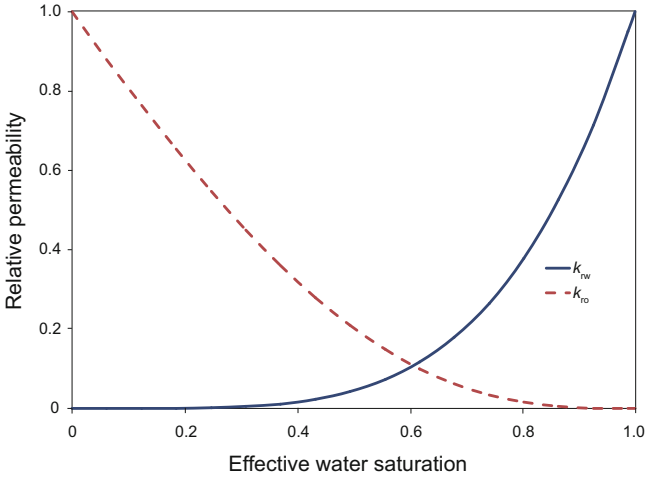

Fig. 12 Relative permeability versus effective water saturation for 3D waterflooding problem

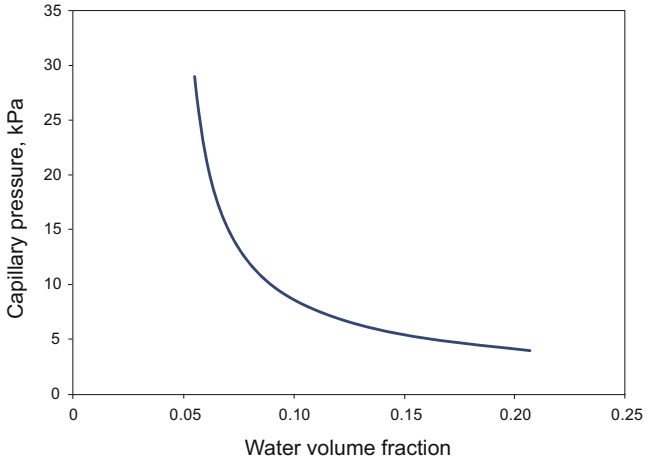

Fig. 13 Capillary pressure versus water volume fraction for 3D waterflooding problem

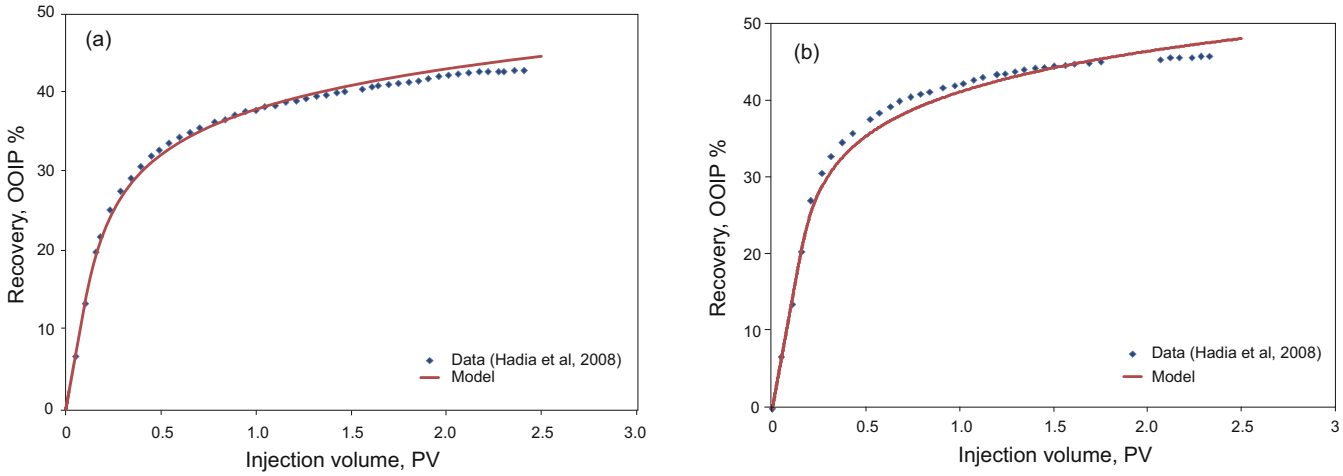

Fig. 14 Numerical and experimental results for recovery performance of OOIP
(a) HP-VI wells and (b) VP-VI wells

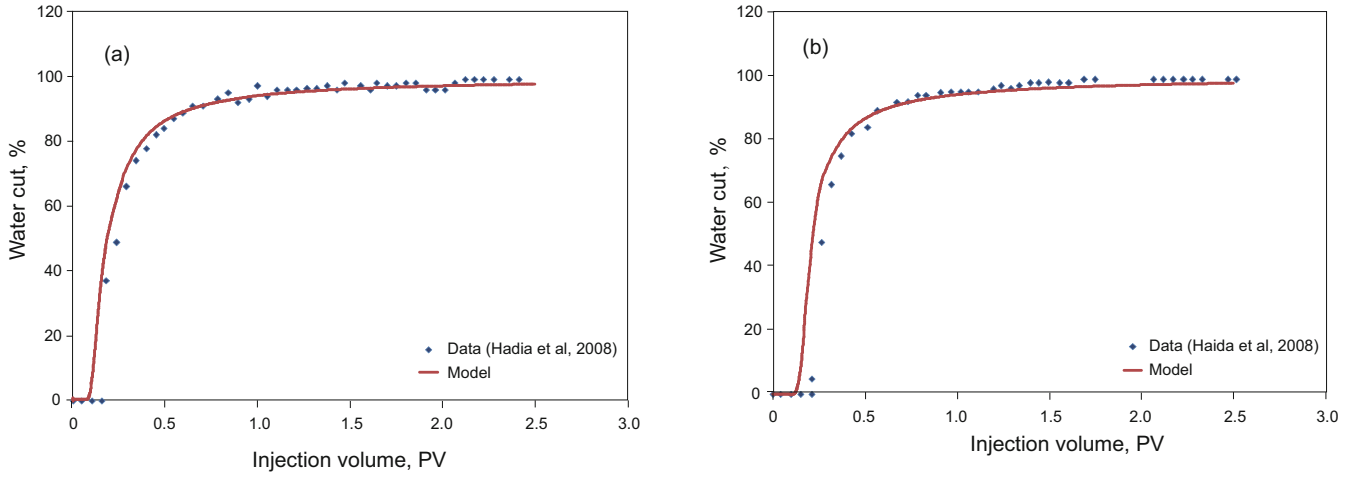

Fig. 15 Comparison of measured and predicted results for water cut curves
(a) HP-VI wells and (b) VP-VI wells

Analytical solution of the case with horizontal discontinuity leads to p=0.167 at the central node of the domain and w_z=16.667 (fluid velocity) for both parts A and B. For the case with vertical discontinuity, exact solution for the nodal pressure at the central node of the domain is p=0.5, while the exact fluid velocities for parts A and B are w_z=10 and 50, respectively. These results are exactly produced by the proposed numerical method for both cases, even with the extremely coarse meshes shown in Fig. 18.

5.4 Confined flow between two perpendicular barriers

In this example, a 100×100×1 m^3 domain with two perpendicular barriers, consisting of extremely low permeability zones, is considered (Fig. 19). The geometry of this example is chosen to be similar to that of Carvalho et al (2007). The domain is saturated with 28% water and 72% oil, at its initial condition. Initial zero pressure is assumed inside the domain. In order to sweep the oil from the domain, water is injected at the right-hand side of the domain with a rate of 8 m^3/day, while the mixture of oil and water is produced at the left-hand side. The absolute permeability is considered 1.5 D inside the barriers and 15,000 D in the rest of the domain. In such a way, permeability inside the barriers changes four orders of magnitude compared with the rest of the reservoir. In fact, these barriers produce a channel, and fluids must preferentially flow inside the channel. The porosity, fluids properties, irreducible water saturation, capillary curve and relative permeability curves are assumed same as example 2 for both of the zones.

Fig. 20 shows the pressure and velocity fields in the domain at t=10 and t=50 days. Fig. 21 shows the water saturation contours at t=10 and t=50 days.

5.5 Five-spot waterflooding problem with a central high permeability zone

In this example, a quarter of five-spot waterflooding problem with a central high permeability zone, is simulated

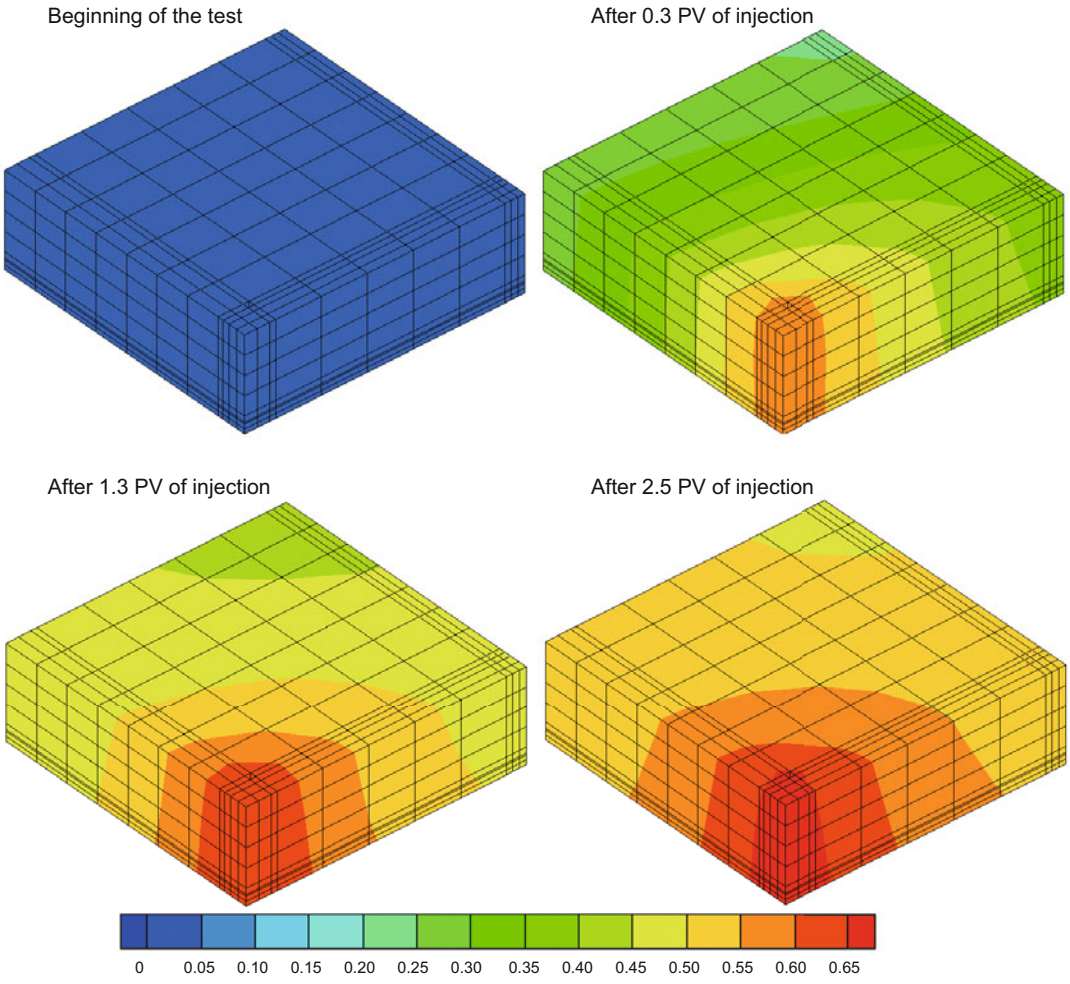

Fig. 16 Distribution of water saturation in the core sample during the test (for HP-VI wells)

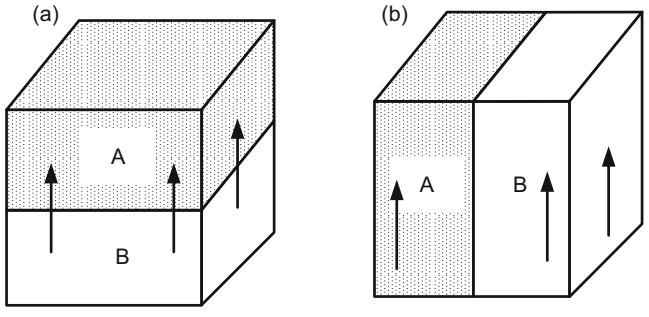

Fig. 17 Cubic domain of example 3
(a) horizontal material discontinuity and (b) vertical material discontinuity

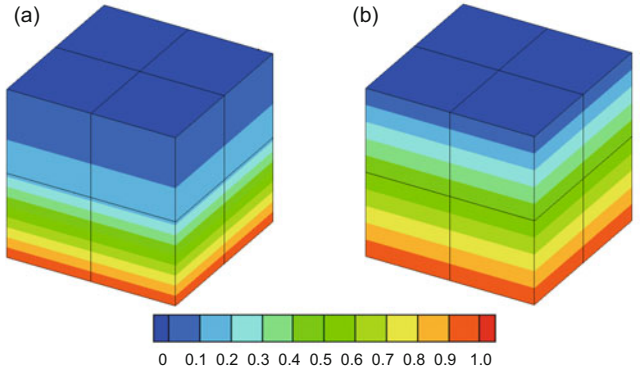

Fig. 18 Pressure distribution inside the cubic domain with extremely coarse mesh (a) for horizontal material discontinuity and (b) for vertical material discontinuity

(Fig. 22). The domain is saturated with 28% water and 72% oil at its initial condition. Initial zero pressure is assumed inside the domain. Water is injected to the domain at a rate of 1,600 liters per day and the model is run for 500 days. The absolute permeability is considered 1,500 D inside the zone with high permeability and 1.5 D in the rest of the domain. Other properties of the fluids and rocks are considered same as example 2.

Fig. 23 shows the water saturation contours after 200 days of injection. At this time, the water front does not reach the high permeability zone, and subsequently, it is not affected by the zone. Therefore, it is expected that before 200 days of water injection, the water front should be similar to that in a homogeneous media. As mentioned by Geiger et al (2004) a good numerical scheme should produce quarter circle shaped

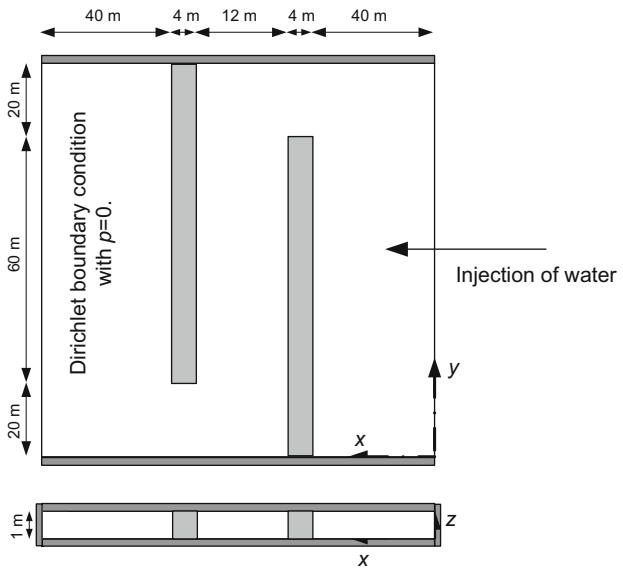

Fig. 19 Geometric configuration of example 4

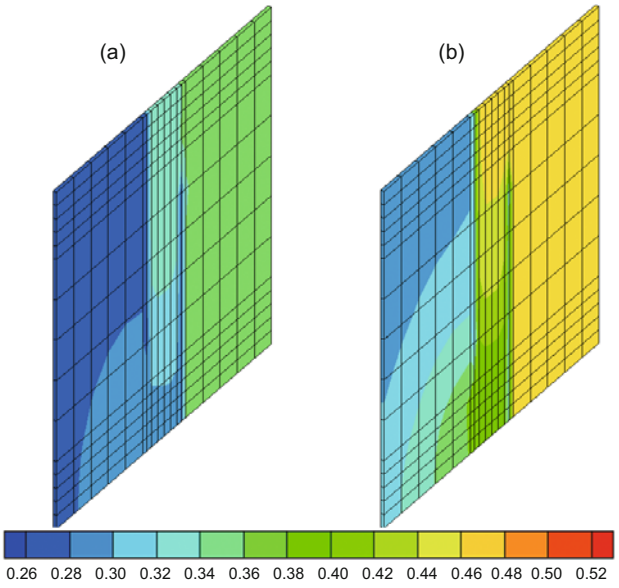

Fig. 21 Water saturation contours of example 4
(a) t=10 days and (b) t=50 days

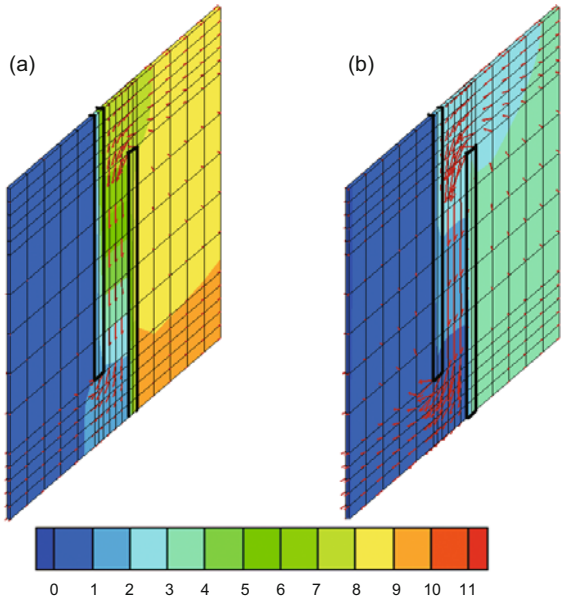

Fig. 20 Pressure and velocity fields of example 4
(a) t=10 days and (b) t=50 days

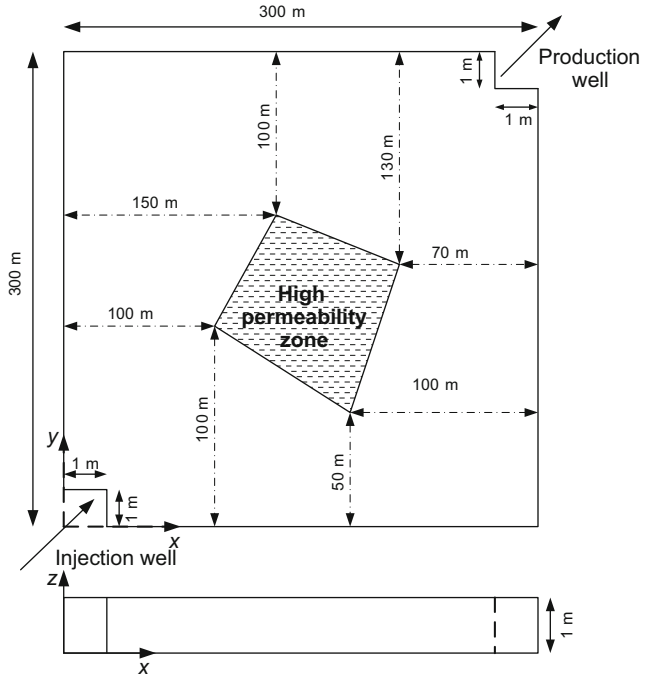

Fig. 22 Geometric configuration of example 5

saturation fronts of the water phase for a five-spot problem in a homogeneous medium. This quarter circle shaped of water front is also produced with the proposed method (Fig. 23).

Fig. 24 shows the water saturation contours after 500 days of injection. At this time, the water front passed the boundary of the zone of high permeability materials, and consequently, the water flow is concentrated at this zone.

6 Conclusions

A control volume finite element method is proposed for the solution of governing differential equations of immiscible two-phase flow in porous media. In this method, the mesh flexibility of finite element method is combined with the local conservative characteristic of finite difference method at the control volume level. The formulation is presented at the element level. The element-wise discretization of the governing equations leads the proposed method to handle the heterogeneity and discontinuity of rock properties in an elegant and accurate manner. The numerical diffusion and dispersion errors at shock fronts are minimal in the proposed method. Subsequently, the proposed solution could accurately preserve the shock fronts. The accuracy and ability of the proposed model was verified with some waterflooding experiments and some representative model examples.

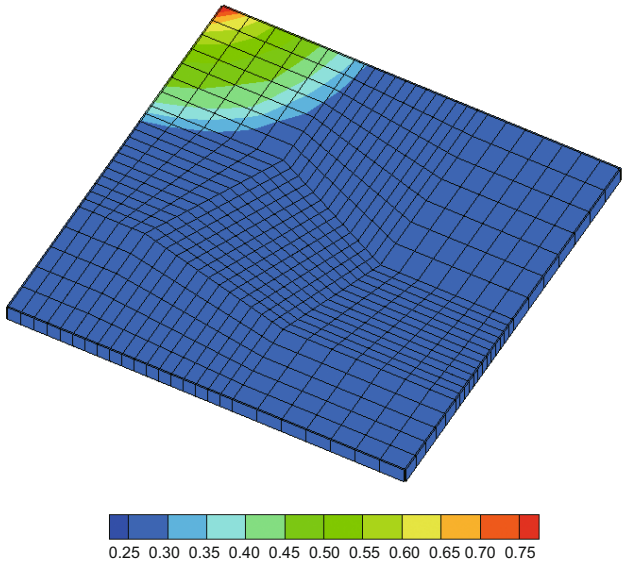

Fig. 23 Water saturation contours of example 5 at 200 days

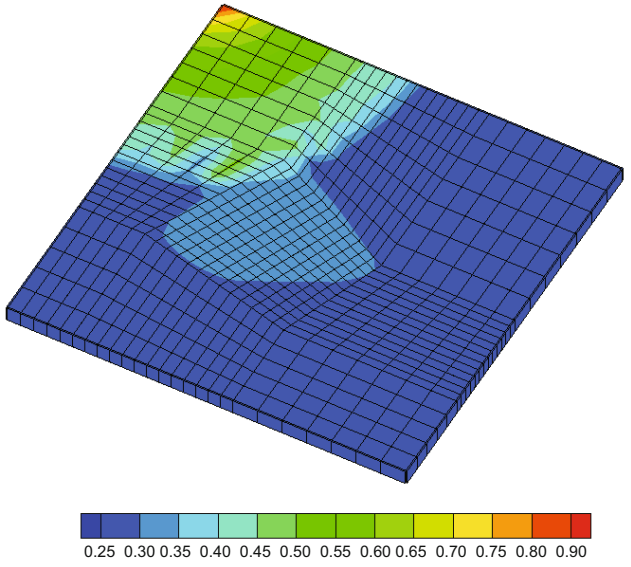

Fig. 24 Water saturation contours of example 5 at 500 days

Acknowledgements

The authors would like to thank Iranian Offshore Oil Company (IOOC) for financial support of this work.

References

Abriola L and Pinder G. A multiphase approach to the modeling of porous media Contamination by organic compounds, 2, Numerical simulation. Water Resource Research. 1985. 21(1): 19-26

Ataie-Ashtiani B and Raeesi-Ardekani D. Comparison of numerical formulations for two-phase flow in porous media. Geotechnical and Geological Engineering. 2010. 28: 373-389

Bergamaschi L, Mantica S and Manzini G. A mixed finite element-finite volume formulation of the black-oil model. Journal of Scientific Computing. 1998. 20(3): 970-997

Brooks R and Corey A. Properties of porous media affecting fluid flow. Journal of the Irrigation and Drainage Division.1966. 92(IR2): 61-88

Carvalho D, Willmersdorf R, and Lyra P. A node-centred finite volume formulation for the solution of two-phase flows in non-homogeneous porous media. International Journal of Numerical Methods in Fluids. 2007. 53: 1197-1219

Chen Z and Ewing R. Comparison of various formulations of three-phase flow in porous media. Journal of Computional Physics. 1997. 132: 362-373

Chen Z, Huan G and Wang H. Simulation of a compositional model for multiphase flow in porous media. Numerical Methods for Partial Differential Equations. 2005. 21: 726-741

Chen Z, Huan G and Ma Y. Computational Methods for Multiphase Flows in Porous Media. Philadelphia: SIAM. 2006a

Chen Z, Huan G and Wang H. Computer simulation of compositional flow using unstructured control volume finite element methods. Computing. 2006b. 78: 31-53

Durlofsky L. Accuracy of mixed and control volume finite element approximations to Darcy velocity and related quantities. Water Resource Research. 1994. 30: 965-973

Edwards M. Unstructured control-volume distributed, full tensor finite-volume schemes with flow based grids. Computational Geosciences. 2002. 6: 433-445.

Edwards M and Rogers C. Finite volume discretization with imposed flux continuity for the general tensor pressure equation. Computational Geosciences.1998. 2: 259-290

Ewing R. The mathematics of Reservoir Simulation. Philadelphia: SIAM. 1983

Fung L, Hiebert A and Nghiem L. Reservoir simulation with a control volume finite element method. Paper SPE 21224 presented at the 11th SPE Symposium on Reservoir Simulation, 17-20 February 1991, Anaheim

Geiger S, Roberts S, Mattha S, et al. Combining finite element and finite volume methods for efficient multiphase flow simulations in highly heterogeneous and structurally complex geologic media. Geofluids. 2004. 4: 284-299

Goodman M and Gowin S C. A continuum theory for granular materials. Archive for Rational Mechanics and Analysis. 1972. 44: 249-266

Hadia N, Chaudhari L, Aggarwal A, et al. Experimental and numerical investigation of one dimensional waterflooding in porous reservoir. Experimental Thermal Fluid Science. 2007. 32: 355-361

Haida N, Chaudhari L, Mitra S, et al. Waterflooding profiles and oil recovery with vertical and horizontal wells. Energy Sources, Part A. 2008. 30: 1604-1618

Hassanizadeh S and Gray W. Thermodynamic basic of capillary pressure in porous media. Water Resource Research. 1993. 29: 3389-3405

Hoteit H and Firoozabadi A. Multicomponent fluid flow by discontinuous Galerkin and mixed methods in unfractured and fractured media. Water Resource Research. 2005. 41(11): W11412

Korsawe J, Perau E, Potthoff S, et al. Numerical approximation of water-air two-phase flow by the mixed finite element method. Computers and Geotechnics. 2003. 30: 695-705

Lewis R, Schrefler B and Rahman N. A finite element analysis of multiphase immiscible flow in deforming porous media for subsurface systems. Communications in Numerical Methods in Engineering. 1998. 14: 135-149

Li B, Chen Z and Huan G. The sequential method for the black oil model on unstructured grids. Journal of Computational Physics. 2003. 192: 36-72

Li X, Liu Z and Lewis R. Mixed finite element method for coupled thermo-hydro-mechanical process in poro-elasto-plastic media at large strains. International Journal for Numerical Methods in Engineering. 2005. 64: 667-708

Lu B and Wheeler M. Iterative coupling reservoir simulation on high performance computers. Petroleum Science. 2009. 6: 43-50

Lujan C. Three-phase flow analysis of NAPL spills in partially water-saturated soils. Ph.D. Dissertation. Colorado State University. 1985

Mello U T, Rodrigues J R and Rossa A L. A control-volume finite-element method for three-dimensional multiphase basin modeling. Marine and Petroleum Geology. 2009. 26: 504-518

Nayagum D, Schafer G and Mose R. Modelling two-phase incompressible flow in porous media using mixed hybrid and discontinuous finite elements. Computational Geosciences. 2004. 8(1): 49-73

Pao W K, Lewis R W and Masters I. A fully coupled hydro-thermo-mechanical model for black oil reservoir simulation. International Journal for Numerical and Analytical Methods in Geomechchanics. 2001. 25: 1229-1256

Rees I. Development of an edge-based finite volume solver for porous media applications. Ph.D. Thesis. University of Wales/Swansea. 2004

Rees I, Masters I, Malan A, et al. An edge-based finite volume scheme for saturated-unsaturated groundwater flow. Computer Methods in Applied Mechanics and Engineering. 2004. 193: 4741-4759

Settari A and Aziz K. Treatment of nonlinear terms in the numerical solution of partial differential equations for multiphase flow in porous media. International Journal of Multiphase Flow. 1975. 1: 8817-844

Todd M, O'Dell P and Hirasaki G. Methods for increased accuracy in numerical reservoir simulator. SPE Journal. 1972. 12: 515-530

Verma S. Flexible grids for reservoir simulation. Ph.D. Thesis. Department of Petroleum Engineering. University of Stanford. 1996

Wang H, Liang D and Ewing R. An improved numerical simulator for different types of flows in porous media. Numerical Methods for Partial Differential Equations. 2003. 19(3): 343-362

Wua Y and Forsyth P. On the selection of primary variables in numerical formulation for modeling multiphase flow in porous media. Journal of Contaminant Hydrology. 2001. 48: 277-304

(Edited by Sun Yanhua)